Anisotropic Thermal Expansion and Cooperative Invar and Anti-Invar Effects in Mn Alloys

Toshihiko Yokoyama[1,2,*] and Keitaro Eguchi[2]

[1]*Department of Materials Molecular Structure, Institute for Molecular Science, Myodaiji-cho, Okazaki 444-8585, Japan*
[2]*Department of Structural Molecular Science, The Graduate University for Advanced Studies (Sokendai), Myodaiji-cho, Okazaki 444-8585, Japan*

(Received 8 November 2012; published 13 February 2013)

We have investigated thermal expansion of a tetragonal $Mn_{88}Ni_{12}$ alloy by x-ray diffraction, Mn and Ni K-edge extended x-ray-absorption fine-structure spectroscopy, and the computational simulations based on the path-integral effective-classical-potential theory. It is found from the x-ray diffraction that the tetragonal lattice constant c exhibits almost no thermal expansion like an Invar alloy, while the lattice constant a shows even larger thermal expansion than usually expected from anharmonicity, implying significant anisotropy in thermal expansion. The extended x-ray-absorption fine-structure reveals that the Mn local environment is actually tetragonally distorted, while the Ni one retains its inherent cubiclike symmetry. Combined with the computational simulations, it is concluded that large thermal expansion along the a axis originates from the anti-Invar effect, while negligibly small thermal expansion along the c axis originates from the cooperative Invar effect. Namely, the tetragonally distorted more stable antiferromagnetic Mn state gives a significantly smaller (slightly longer) atomic radius along the a (c) axis than the radius of the spherical paramagnetic state.

DOI: 10.1103/PhysRevLett.110.075901 PACS numbers: 65.40.De, 61.05.cj, 61.05.cp, 63.20.Ry

An Invar alloy $Fe_{66}Ni_{34}$ that shows anomalously small thermal expansion over a wide temperature range was discovered by Guillaume in 1897 [1,2]. The Invar effect has been utilized in various kinds of precision tools and instruments such as semiconductor and flat-panel-display manufacturing systems, precise scalers, precise molded imprints, astronomical telescopes, and so forth. A phenomenological model of the Invar effect is that there exist at least two types of electronic states in Fe, typically called high-spin (HS) and low-spin (LS) states [3–6]. In this two-state model, the HS state with a larger atomic radius is slightly more stable at a temperature of 0 K than the LS state. This results in the compensation of thermal expansion due to increasing density of the LS state at higher temperature. Until now, however, there have continued to be extensive discussions concerning the detailed origin of the Invar effect. In recent electronic structure calculations based on the density-functional theory [7], much more complicated electronic structures were proposed, where noncollinear magnetic moments with different magnitudes are distributed, depending on the local environment.

On the other hand, we have very recently investigated thermal expansion [8,9] from a different view point of thermal vibration, by combining temperature-dependent extended x-ray-absorption fine-structure (EXAFS) measurements with the path-integral effective classical potential (PIECP) Monte Carlo (MC) simulations [8–13]. A quantum mechanical dynamical approach that explicitly treats the finite temperature effect and the quantum fluctuation of nuclei should be essentially important for the deeper understanding of thermal properties like the Invar effect. We clarified that the weakness of thermal expansion at low temperature is ascribed to the vibrational quantum effect and that the Ni environment shows small but meaningful thermal expansion, while the Fe one shows almost no thermal expansion.

In this Letter, we will report on cooperative anisotropic thermal expansion, where one axis shows the Invar effect and the other the anti-Invar effect. The sample is a so-called face-centered-tetragonal (fct) antiferromagnetic $Mn_{88}Ni_{12}$ alloy [14–16]. Although in the Bravais lattice body-centered tetragonal (bct) should formally be used, we will here call the crystal lattice fct for simplicity since the MnNi alloys are likely to undergo the phase transition to fcc at high temperature. It is found that thermal expansion along the fct c axis ($c > a$) is negligibly small, while along the a axis it is somewhat larger than usually expected from anharmonicity in the lattice vibration. We have concluded that the two-state model in Mn similar to the Weiss model in the FeNi Invar case is most appropriate to describe the observed cooperative Invar and anti-Invar effects. The Invar and anti-Invar effects of this material could be more easily understandable compared with the FeNi Invar alloy, because the material shows a simple collinear antiferromagnetic structure with the magnetic moments aligned parallel within the (001) plane and antiparallel between the (001) planes [14–16]. It should also be emphasized that the macroscopic thermal expansion does not always coincide with the local thermal expansion. Thermal expansion basically comes from a microscopic origin of anharmonicity in the chemical bonds, and EXAFS is the most suitable method to get a deep understanding of the essence of thermal expansion [11–13,17–21]. In this work, EXAFS has clarified that the local Mn environment is tetragonally distorted as the lattice, while the Ni site maintains cubic symmetry.

Powder XRD measurements of a $Mn_{88}Ni_{12}$ foil 100 μm thick was performed by using Rigaku RINT-UltimaIII in Instrumental Center of Institute for Molecular Science (IMS) in the temperature range of 40–300 K. The Cu $K\alpha$ radiation was employed as a x-ray source and the reflected x rays were monochromatized to eliminate Mn $K\alpha$ x-ray fluorescence. The 113 and 311 diffractions were mainly used to yield the lattice constants a and c. Mn and Ni K edge EXAFS spectra of a pinholeless $Mn_{88}Ni_{12}$ foil 12.5 μm thick were recorded at beam line 9C of Photon Factory in High Energy Accelerator Research Organization (KEK-PF) [22] with the transmission mode using a Si(111) double crystal monochromator. Ionization chambers filled with 30% N_2 in He and 100% N_2 were used to measure the incident and transmitted x-ray intensities, respectively. The measurement temperature range was 11–300 K.

Details of the EXAFS analysis procedure are described in the Supplemental Material [23]. The first-nearest neighbor (NN) shells were analyzed. It is noted that the neighboring Mn and Ni atoms are not distinguished because of only a small difference of the backscattering amplitudes between Mn and Ni, and therefore the resultant values obtained experimentally are the average ones for each x-ray absorbing atom. Because of the tetragonal distortion in the lattice, it is natural to assume the presence of two inequivalent shells in the first-NN coordination. For the backscattering amplitudes and the phase shifts, the FEFF8.4 [24] theoretical standards were employed by conducting the FEFF calculations of clusters assuming some randomly distributed alloy structures as in the following MC simulations. As structural parameters, the bond distance R, the mean square relative displacements $C_2 = \langle (r - R)^2 \rangle$, and the mean cubic relative displacements $C_3 = \langle (r - R)^3 \rangle$ [25] for the two inequivalent contributions in the first-NN shells were obtained. To evaluate the average quantities, the empirical one-shell analysis using the lowest temperature data as a reference was also conducted.

PIECP MC simulations within the low coupling approximation [8–10,12] were performed under a constant number of particles, pressure, and temperature (NPT) condition. The total number of atoms was 500 (5^3 fct unit cells), and the atomic distributions of Mn and Ni were chosen randomly. Twenty types of the superlattices were simulated and the results were finally averaged to provide consequent physical quantities. The atomic potentials of Mn and Ni were described based on the empirical embedded-atom method (EAM) [26,27]. Detailed potential parameters are given in the Supplemental Material [23]. The Ni potential is assumed to have no angular dependence. In Mn, by referring to the previous work [28], two kinds of the potential functions, the LS and HS states, were prepared. Here we use convenient expressions of LS and HS, which could be regarded as antiferromagnetic and paramagnetic states, respectively. In the HS state with a larger atomic radius the potential is spherically symmetric as usual, while the Mn LS state exhibits tetragonal distortion with respect to the principal z axis parallel to the c axis and is more stable than the HS state. The absolute values for the distances in the potential parameters were slightly shifted in the process of the potential optimization to match the present XRD results. We have performed PIECP MC simulations for this two-state model. For comparison, a tetragonal-axis rotatable LS model is also investigated, where the principal axis of the Mn LS state is allowed to incline away from the c axis, with only the LS state permitted. In this model, a Heisenberg-type exchange interaction for the entire first-NN coordination is augmented to stabilize antiferromagnetism. Moreover, we have also examined a tetragonal-axis fixed LS model, where the tetragonal rotational axis is fixed along the c axis with only the LS state permitted, and a classic LS-HS two-state model without the vibrational quantum fluctuations.

Figure 1 shows the temperature dependence of the fct lattice constants a and c and the corresponding thermal expansion along the a and c axes determined by the powder XRD measurement. The c axis is found to be considerably longer than the a axis. This result seems to be inconsistent with the previous report [16], where $c > a$ was observed only when the Ni concentration is larger than ~0.15, and the $Mn_{88}Ni_{12}$ alloy showed $c < a$. The reason for this discrepancy is not clear, but we could expect some difference in the sample preparation procedures

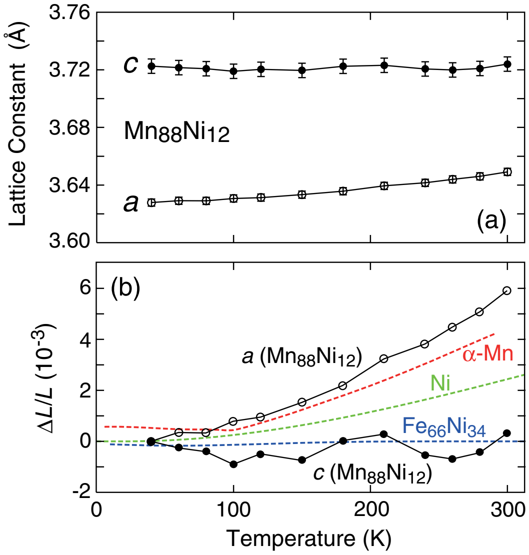

FIG. 1 (color online). Experimental fct lattice constants a and c (a) and corresponding thermal expansion (b) in $Mn_{88}Ni_{12}$ determined by the powder XRD, together with the literature data of α-Mn, fcc Ni, and a $Fe_{66}Ni_{34}$ Invar alloy [38]. Error bars in (b) are omitted.

(the Ni content in the present sample was verified to be 0.12 from the relative x-ray absorption intensities between Mn and Ni). In Fig. 1, the thermal expansion along the a axis is found to be much larger than that along the c axis, exemplifying large anisotropic thermal expansion. Thermal expansion along the a axis seems somewhat larger than usually expected from anharmonicity in the potential, while that along the c axis is as small as that in the Invar alloy. This finding may be indicative of anisotropic thermal expansion due to the cooperative Invar-anti-Invar effects.

Figure 2 gives the bond distances around Mn and Ni determined by EXAFS. Because of the tetragonal lattice, we have tried a two-shell fitting, in which longer (l) bonds within the bc and ca planes and shorter (s) bonds within the ab plane exist with coordination numbers N of 8 and 4, respectively. The EXAFS analysis clearly shows that the environment around Mn is really tetragonally distorted with meaningfully different bond distances between Mn(l) and Mn(s). Strictly speaking, the two kinds of bonds observed by EXAFS are poorly defined since the longer and shorter bonds are overlapped with each other especially at higher temperature due to thermal vibration. One cannot always clearly distinguish the two inequivalent bonds with large vibrational amplitudes by one-dimensional EXAFS information. In the present work, however, by comparing the EXAFS results to the PIECP simulated ones given below, two kinds of the inequivalent shells determined by EXAFS are found to be successfully ascribed to the longer (within the bc or ca plane) and the shorter (within the ab plane) bonds. On the other hand, the environment around Ni is regarded as cubic because of a negligible difference between Ni(l) and Ni(s). This consequence is also confirmed by the one-shell analysis, which yields a goodness of fit, χ_ν^2, of as much as 53.9 for Mn but 6.8 for Ni, implying that the one-shell fit is sufficient for Ni. It is noted that although the crystal system is purely fct, the local structure does not coincide with the lattice as in other disordered alloy systems, allowing cubic symmetry around Ni in this alloy. This will be discussed further below in terms of the Debye-Waller factors.

Figure 3 shows the binding energies of fcc LS-HS and fct LS $Mn_{88}Ni_{12}$ lattices at a temperature of 0 K as a function of the lattice constant, calculated by using the present potential functions. In the atomic potentials employed, fcc $Mn_{88}Ni_{12}$ exhibits a more stable LS state by 12.0 meV than the HS state with the average lattice constants of $a_{\text{fcc}}^{\text{LS}} = 3.685$ Å and $a_{\text{fcc}}^{\text{HS}} = 3.721$ Å. By introducing the tetragonal distortion for the Mn LS state, the equilibrium lattice constants become $a_{\text{fct}}^{\text{LS}} = 3.644$ Å and $c_{\text{fct}}^{\text{LS}} = 3.733$ Å, respectively. The resultant distance within the ab plane is considerably shorter than that of the Mn HS state, while the one along the c axis is a little longer than the HS one.

Figure 4 gives the simulated results for the bond distances and the lattice constants by adopting the four models described above. The simulated Mn(l) and Mn(s) means the bonds within the fct bc or ca planes and the ab plane, respectively. It is clearly found that the LS-HS two-state model successfully reproduces the lattice constants as well as the bond distances. In the tetragonal-axis rotatable LS model, the calculated lattice constant c gradually decreases with temperature, while the experiment shows nearly no thermal expansion. The simulated behavior in this model can qualitatively be understood; the inclination of the z axis with respect to the [001] axis simply gives a smaller lattice constant of c, resulting from the rotation of the principal axis. In the tetragonal-axis fixed LS model, where only the Mn LS state is allowed and the Mn axis is fixed at [001], thermal expansion of the lattice constant a is estimated to be too small compared to the experiments. The classic LS-HS model is rather good, but the lattice constants are erroneously temperature dependent even at low

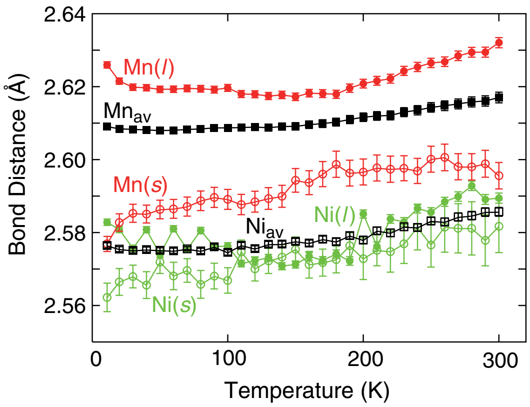

FIG. 2 (color online). Experimental bond distances in $Mn_{88}Ni_{12}$ determined by the Mn and Ni K-edge EXAFS. l, s, and av denote the longer and shorter bonds and the average, respectively.

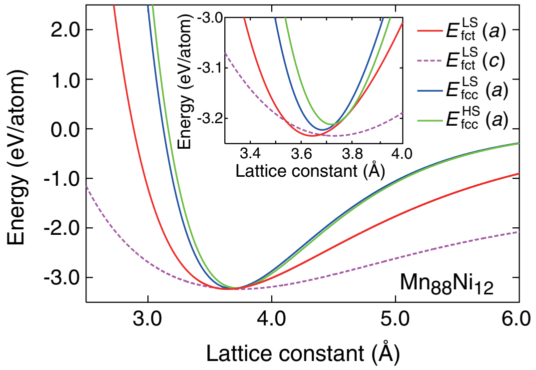

FIG. 3 (color online). Binding energies of fcc LS-HS and fct LS $Mn_{88}Ni_{12}$ as a function of the lattice constant at a temperature of 0 K. The plots for the fct lattice, $E_{\text{fct}}(a)$ and $E_{\text{fct}}(c)$ are given by fixing $c_{\text{fct}}^{\text{LS}} = 3.733$ Å and $a_{\text{fct}}^{\text{LS}} = 3.644$ Å, respectively. The inset is the magnified picture.

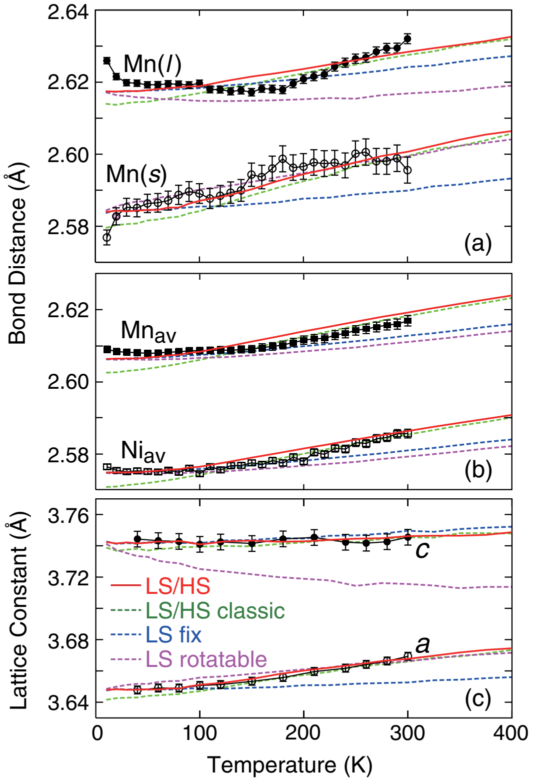

FIG. 4 (color online). Simulated bond distances for (a) Mn(l) and Mn(s) and (b) Mn$_{av}$ and Ni$_{av}$, and (c) fct lattice constants a and c, together with the experimental EXAFS and XRD data with error bars. Four kinds of simulated results are depicted: the quantum LS-HS model (red solid line), the classic LS-HS model (green dashed), the tetragonal-axis fixed LS model (blue dashed), and the tetragonal-axis rotatable model (purple dashed).

temperature, implying the importance of the vibrational quantum effect. In the quantum mechanical LS-HS model, the bond distances as well as the lattice constants agree rather well with the experimental results. This confirms that the two inequivalent bonds in EXAFS are regarded as the bonds within the *bc* or *ca* plane and *ab* plane. Consequently, the present anisotropic thermal expansion is explained by the cooperative Invar and anti-Invar effects in the Mn atom, where the tetragonally distorted more stable LS Mn state gives a smaller atomic radius within the *ab* plane and a larger radius along the *c* axis rather than the spherical one of the HS state.

Let us briefly discuss higher-order cumulants. For details, see Supplemental Material [23]. In both C_2 and C_3 (overall values for the average first NN shells), temperature dependent behaviors are well reproduced by the computational simulations based on the LS-HS model. The Debye model [29] yields the Debye temperatures of 428 (Ni) and 426 K (Mn), which are reasonably identical within the errors. The temperature-independent static disorder C_2^s is estimated as 1.38×10^{-3} Å^2 (Ni) and 0.99×10^{-3} Å^2 (Mn). In spite of the fact that the EXAFS analysis reveals the tetragonal distortion of the Mn local structure and the cubiclike symmetry around Ni, the overall C_2^s is found to be slightly larger in Ni than in Mn. This indicates larger random structural disorder around Ni, which cannot be categorized into two inequivalent shells like Mn. The bond angle variance around Ni should be larger in Mn. Temperature-dependent C_3 is ascribed to anharmonicity in the potential functions and the temperature-independent static C_3^s is found to be quite small. In the Mn environment, C_2^s and C_3^s are considered to originate from the intrinsic difference in the bond distances between Mn(l) and Mn(s) and also in Mn-Mn and Mn-Ni.

In summary, we have investigated thermal expansion of fct Mn$_{88}$Ni$_{12}$ by the XRD and EXAFS experiments and the PIECP simulations. The fct lattice constant a ($a < c$) shows somewhat larger expansion than usual, while the lattice constant c exhibits almost no expansion. This behavior is explained by the cooperative Invar and anti-Invar effects in the Mn atom, where the tetragonally distorted Mn state coupled antiferromagnetically to the neighboring atoms is more stable than the spherical paramagnetic HS state and resultantly gives a significantly smaller atomic radius within the *ab* plane and a slightly larger radius along the *c* axis than the spherical one of the HS state. The present observation is not a rare case, but similar behaviors can be seen in Mn$_{87}$Pd$_{13}$ [14] and Mn$_{85}$Zn$_{15}$ [15], although no discussion of these has been made so far. Interestingly, a contrasting behavior, where a longer (shorter) axis is compressed (expanded) as in the tetragonal-axis rotatable model in the present simulation, can be found in Mn$_{80}$Ni$_{20}$ and Mn$_{80}$Ga$_{20}$ [15]. In Mn$_{88}$Ni$_{12}$, the Mn atoms are tetragonally distorted associated with the lattice distortion, while Ni atoms retain cubic symmetry. From the local point of view, it is not unusual that different structural behaviors in randomly distributed different elements are observed. It should be noted that XRD gives only the average structure and the local structure is not always the same in the random-alloy–solid-solution systems. Recently, there have been reports of several kinds of metal alloys that exhibit anomalous properties like negative or zero thermal expansion [30–37]. Since these works have been performed based on the lattice expansion, it will be interesting to investigate the thermal expansion from the present view point of the local structure.

We thank Mr. Motoyasu Fujiwara of IMS for his great help in the XRD measurements in the Instrument Center of IMS. We are also grateful for the partial financial support of Grant-in-Aid for Scientific Research (A) (No. 22241029) from the Japan Society for the Promotion of Science (JSPS). The EXAFS measurements at the Photon Factory have been performed under the approval of the Photon Factory Program Advisory Committee (PF-PAC No. 2012G008).

*yokoyama@ims.ac.jp

[1] C. E. Guillaume, C.R. Hebd. Seances Acad. Sci. **125**, 235 (1897).

[2] E. F. Wasserman, *Ferromagnetic Materials*, edited by K. H. J. Bushow and E. P. Wohlfarth (Elsevier Science Publishers B.V., New York, 1990), Vol. 5, p. 237.

[3] R. J. Weiss, Proc. R. Soc. A **82**, 281 (1963).

[4] M. Shiga, J. Phys. Soc. Jpn. **22**, 539 (1967).

[5] M. Matsui and S. Chikazumi, J. Phys. Soc. Jpn. **45**, 458 (1978).

[6] S. Chikazumi, J. Magn. Magn. Mater. **10**, 113 (1979).

[7] M. van Schilfgaarde, I. A. Abrikosov, and B. Johansson, Nature (London) **400**, 46 (1999).

[8] T. Yokoyama and K. Eguchi, Phys. Rev. Lett. **107**, 065901 (2011).

[9] T. Yokoyama, J. Surf. Sci. Nanotech. **10**, 486 (2012).

[10] A. Cuccoli, R. Giachetti, V. Tognetti, R. Vaia, and P. Verrucchi, J. Phys. Condens. Matter **7**, 7891 (1995), and references therein.

[11] T. Fujikawa, T. Miyanaga, and T. Suzuki, J. Phys. Soc. Jpn. **66**, 2897 (1997).

[12] T. Yokoyama, Phys. Rev. B **57**, 3423 (1998).

[13] T. Yokoyama, J. Synchrotron Radiat. **8**, 87 (2001).

[14] T. J. Hicks, A. R. Pepper, and J. H. Smith, J. Phys. C **1**, 1683 (1968).

[15] H. Uchishiba, J. Phys. Soc. Jpn. **31**, 436 (1971).

[16] N. Honda, Y. Tanji, and Y. Nakagawa, J. Phys. Soc. Jpn. **41**, 1931 (1976).

[17] A. Di Cicco, A. Trapananti, S. Faggioni, and A. Filipponi, Phys. Rev. Lett. **91**, 135505 (2003).

[18] H. Wende, D. Arvanitis, M. Tischer, R. Chauvistre, H. Henneken, F. May, and K. Baberschke, Phys. Rev. B **54**, 5920 (1996).

[19] G. Dalba, P. Fornasini, R. Grisenti, and J. Purans, Phys. Rev. Lett. **82**, 4240 (1999).

[20] D. Cao, F. Bridges, G. R. Kowach, and A. P. Ramirez, Phys. Rev. Lett. **89**, 215902 (2002).

[21] P. Fornasini, S. a Beccara, G. Dalba, R. Grisenti, A. Sanson, M. Vaccari, and F. Rocca, Phys. Rev. B **70**, 174301 (2004).

[22] M. Nomura, http://pfxafs.kek.jp/?lang=en.

[23] See Supplemental Material at http://link.aps.org/supplemental/10.1103/PhysRevLett.110.075901 for details of EXAFS analyses and MC simulations.

[24] A. L. Ankudinov, B. Ravel, J. J. Rehr, and S. D. Conradson, Phys. Rev. B **58**, 7565 (1998).

[25] G. Bunker, Nucl. Instrum. Methods Phys. Res. **207**, 437 (1983).

[26] M. S. Daw and M. I. Baskes, Phys. Rev. B **29**, 6443 (1984).

[27] S. M. Foiles, Phys. Rev. B **32**, 3409 (1985).

[28] Y.-M. Kim, Y.-H. Shin, and B.-J. Lee, Acta Mater. **57**, 474 (2009).

[29] G. Beni and P. M. Platzman, Phys. Rev. B **14**, 1514 (1976).

[30] A. Martínez, J. Spottorno, A. I. Figueroa, F. Bartolome, L. M. Garcia, C. Prestipino, A. Hernando, and P. Crespo, Phys. Rev. B **82**, 012406 (2010).

[31] A. Martínez, J. J. Romero, F. Bartolome, L. M. Garcia, F. Baudelet, A. Hernando, and P. Crespo, Appl. Phys. Lett. **101**, 022412 (2012).

[32] S. Iikubo, K. Kodama, K. Takenaka, H. Takagi, M. Takigawa, and S. Shamoto, Phys. Rev. Lett. **101**, 205901 (2008).

[33] S. Iikubo, K. Kodama, K. Takenaka, H. Takagi, and S. Shamoto, Phys. Rev. B **77**, 020409 (2008).

[34] K. Takenaka and H. Takagi, Appl. Phys. Lett. **94**, 131904 (2009).

[35] C. Wang, L. Chu, Q. Yao, Y. Sun, M. Wu, L. Ding, J. Yan, Y. Na, W. Tang, G. Li, Q. Huang, and J. W. Lynn, Phys. Rev. B **85**, 220103(R) (2012).

[36] P. Gorria *et al.*, Phys. Rev. B **80**, 064421 (2009).

[37] P. Gorria, R. Boada, A. Fernández-Martínez, G. Garbarino, R. I. Smith, J. Chaboy, J. I. García Alonso, D. Martínez-Blanco, G. R. Castro, M. Mezouar, A. Hernando, and J. A. Blanco, Phys. Status Solidi **3**, 115 (2009).

[38] *Thermophysical Properties of Matter*, edited by Y. S. Touloukian, R. K. Kirby, R. E. Taylor, and P. D. Desai (Plenum, New York, 1975), Vol. 12.